Available online at www.sciencedirect.com
SCIENCE DIRECT®
Journal of Catalysis 222 (2004) 565–571
JOURNAL OF CATALYSIS
www.elsevier.com/locate/jcat

Research Note

TiO_2 and ZrO_2 crystals in SBA-15 silica: performance of $Pt/TiO_2(ZrO_2)$/SBA-15 catalysts in ethyl acetate combustion

Xueguang Wang,[a] M.V. Landau,[a,*] H. Rotter,[a] L. Vradman,[b] A. Wolfson,[a,b] and A. Erenburg [a]

[a] *Blechner Center for Applied Catalysis and Process Development, Chemical Engineering Department, Ben-Gurion University of the Negev, Beer-Sheva, 84105, Israel*

[b] *Chemical Engineering Department, Negev Academic College of Engineering, Beer-Sheva, 84100, Israel*

Received 20 August 2003; revised 20 November 2003; accepted 2 December 2003

Abstract

TiO_2 (40–64 wt%) and ZrO_2 (48–62 wt%) were inserted in SBA-15 mesostructured silica by chemical solution decomposition or hydrolysis of the corresponding alkoxides inside the host pores. It yielded composites with 85–94% TiO_2 crystallinity (anatase) and > 95% crystallinity of ZrO_2 (tetragonal phase). The 4.5 nm (ZrO_2) or 5.0 and 8.5 nm (TiO_2) nanocrystals did not block the SBA-15 pores, and their surface was fully accessible for adsorbed nitrogen or ethyl acetate molecules. After deposition of 0.3 wt% Pt the activity of Ti(Zr)O_2/SBA-15 materials in ethyl acetate combustion was proportional to the surface area of the corresponding transition metal oxide nanoparticles, being a function of their loading and crystal size. The platinized composite materials displayed 1.7–3 times higher activity compared with platinum on bulk Ti(Zr)O_2 oxides prepared by the same methods and two orders of magnitude higher activity relative to Pt/SBA-15 and Pt/γ-Al_2O_3 catalysts.

Keywords: Mesostructured silica; Titania; Zirconia; Platinum; Ethyl acetate; Combustion; Nanocrystals

1. Introduction

Ordered mesoporous silicas (OMS) with adjustable pore sizes and close to maximal possible surface areas [1,2] provide wide opportunities for synthesis of advanced catalytic materials with different chemical functionalities [3,4]. Various catalytic phases (CP) such as metals, modified pure and mixed oxides, sulfides, and heteropoly compounds could serve as a "functionalization source" being assembled in the pore system of OMS as nanoparticles with a distinct structure. However, success in such preparations requires high CP loading (> 30 wt%) needed for compensation of the matrix dilution effect and the location of CP nanoparticle ensembles inside the hosts pore system with its minimal blocking and high CP crystallinity [5]. Yet the simultaneous accomplishment of these requirements is a very complicated practical problem. Thus, only few examples of successful preparations of CP/OMS catalytic materials are reported that substantially excel in the performance of the corresponding CP on common supports like silica-gels or bulk CP. Among them are Fe_2O_3/MCM-41 for SO_2 oxidation in highly concentrated gases [6], WS_2/SBA-15 for hydrotreatment of dibenzothiophene [5], SO_4–ZrO_2/SBA-15 for acid-catalyzed reactions [7], and phosphotungstic heteropolyacid/SBA-15 for benzene alkylation with *n*-decene [8].

Three preparations of advanced TiO_2/OMS catalytic materials containing anatase modifications as CP were recently reported and their performance was tested in the photooxidative degradation of pollutants in wastewater [9–11]. Though the CP dispersion and loading were high, especially in [11], the catalytic activity of the composite materials did not exceed that of bulk TiO_2. This could be a result of competing effects of effective particle size on charge–carrier dynamics (electron–hole recombination rate) and amount of available surface active sites, so that decreasing the TiO_2 crystal size to less than 10–25 nm decreases the quantum yield in photocatalytic reactions and hence catalytic activity [12,13].

VOC combustion is another important reaction in environmental protection technology [14]. Noble metals supported on several transition metal oxides such as chro-

* Corresponding author.
E-mail address: mlandau@bgumail.bgu.ac.il (M.V. Landau).

0021-9517/$ – see front matter
doi:10.1016/j.jcat.2003.12.003

mia [15], titania [16], and zirconia [17] were already tested as catalysts for various VOC combustions. It yielded better catalysts compared with noble metals supported on common silica or alumina. Recently Verykios et al. demonstrated that TiO_2 in anatase or rutile forms decomposes ethyl acetate (EA), one of the most recalcitrant VOC, in the presence of oxygen mainly to acetic acid, ethanol, acetaldehyde, and ethylene [16]. The authors proved that EA degradation is the rate-determining step in EA combustion over Pt/TiO_2 catalysts. Thus, increasing the surface area of the TiO_2 phase by assembly of its nanocrystals in OMS hosts could increase the EA decomposition efficiency and consequently the catalytic performance of Pt/TiO_2 catalysts for VOC combustion.

Here we report a novel successful example of catalysis by embedded TiO_2 and ZrO_2 CP as nanocrystal ensembles inside SBA-15 OMS. In the present work it was demonstrated that the activity of platinum supported on TiO_2 anatase and tetragonal ZrO_2 phases in EA combustion is proportional to the surface area of the corresponding oxides, being a function of their loading and crystal size.

2. Experimental

2.1. Catalyst preparation

SBA-15 was prepared according to procedure [18] by crystallization from acidic aqueous solutions of poly(ethylene glycol)–*block*-poly(propylene glycol)–*block* poly(ethylene glycol) copolymer (Aldrich, $M_{avg} = 5800$) and TMOS. The procedure was modified to reduce the microporosity by increasing the duration of the hydrothermal treatment [5].

A TiO_2 phase was inserted into SBA-15 by two methods: chemical solution decomposition (CSD) and internal hydrolysis (IH) while ZrO_2 was inserted only by CSD. The CSD of both oxides was performed similarly to the procedure described in [7] for ZrO_2. All chemicals were purchased from Aldrich. The CSD of alkoxides fixed the TiO_2 or ZrO_2 phase inside the channels of SBA-15. The saturated pressure of solvent outside the pores excluded its evaporation and prevented pulling out the Ti(Zr)-alkoxide solution by capillary forces. Typically, 1 g of SBA-15 was impregnated with a Ti[*n*-BuO]$_4$ solution (80 wt%) in *n*-decane or Zr(*n*-PrO)$_4$ solution (70 wt%) in *n*-PrOH under a N_2 atmosphere in a glove box. After separation of the excess solution by filtration, the wet solid in a 50 cm^3 glass was placed in a 1-L autoclave that contained 45 cm^3 of pure solvent (*n*-decane or *n*-PrOH). The CSD was conducted for 3 h at 573 K (TiO_2) or 493 K (ZrO_2) (5 K/min). After cooling and discharging, the solid was dried under vacuum at 423 K for 2 h followed by calcination at 773 K in air for 2 h. Unsupported TiO_2 in anatase form and ZrO_2 in tetragonal form were prepared following the same procedure and performing the CSD step in the absence of SBA-15. Another bulk reference ZrO_2 sample was commercially obtained from Norton Corp. (Material XZ16075).

The insertion of a TiO_2 phase to the SBA-15 host by the IH method was performed by hydrolysis of Ti(*n*-BuO)$_4$ in *n*-decane solution inside the silica nanotubes. In a typical preparation 1 g of SBA-15 was impregnated with a 80% Ti[*n*-BuO]$_4$ solution in *n*-decane in a glove box. After separation of the excess solution by filtration, the wet solid was placed in a glass filled with 50 cm^3 distilled water and stirred vigorously at room temperature for 24 h. Next, the solid was separated from the water phase by filtration, dried under vacuum at 423 K for 24 h, and calcined at 773 K in air for 2 h. Negligible solubility of *n*-decane in water excluded the deposition of Ti-hydroxide outside SBA-15 pores. In order to obtain TiO_2 loadings higher than 45 wt% the IH procedure was repeated one or two times after the hydrolysis step and drying. It was followed by a single calcination of the final material. The reference unsupported TiO_2 was prepared by the same procedure, with the hydrolysis (H) step performed in the absence of SBA-15.

Finally, 0.3 wt% Pt was deposited on the supported and unsupported transition metal oxides, as well as on pure SBA-15 and commercial γ-Al_2O_3 (Norton SA 6175, 270 m^2/g) reference supports. The amount of 1.2 g of the corresponding supporting materials was inserted into 35 cm^3 of an aqueous solution of H_2PtCl_6 (0.102 mg Pt/ml). The mixture was stirred at room temperature for 2 h followed by evaporation at 373 K for 2 h and drying at 383 K for 12 h. Catalyst activation was performed before testing in a hydrogen flow of 100 ml/min at 573 K for 2 h. This procedure yields high Pt dispersion in Pt/TiO_2 catalysts even with low surface areas (< 30 m^2/g) at < 1.0 wt% Pt loadings [16,23].

2.2. Catalyst characterization

The chemical composition of solid catalysts (wt%) was measured by energy dispersive X-ray spectroscopy (EDS) analysis with a JEOL JEM 5600 scanning electron microscope (SEM). The SEM images of SBA-15 material and $TiO_2(ZrO_2)$/SBA-15 composites were obtained from the same instrument equipped with element mapping after the samples were coated with gold using an ion sputter system. Surface areas, pore volumes, and pore-size distributions were obtained from N_2-adsorption–desorption isotherms using conventional BET and BJH methods. The samples were outgassed under vacuum at 523 K. Isotherms were obtained at the temperature of liquid nitrogen with a NOVA-2000 (Quantachrome, Version 7.02) instrument.

Conventional wide-angle XRD and SAXS patterns were obtained on a Phillips diffractometer PW 1050/70 (Cu-K_α radiation) equipped with a graphite monochromator using software developed by Crystal Logic. SAXS patterns were recorded with the narrow X-ray beam. The data were obtained with a 0.02° step size, 2 s at each step. The ZrO_2 and TiO_2 crystal domain sizes were determined using the Scherrer equation $h = K\lambda/[(B^2 - \beta^2)^{0.5}\cos(2\theta/2)]$, where $K = 1.000$ is the shape factor; $\lambda = 0.154$ nm; β is the instrumental broadening correction; B is the (101), (112), (200),

(103), (211), and (202) reflections broadening at $2\theta = 30.2$, 50.3, 50.6, 59.6, 60.0, and 62.8° for ZrO_2 (Powder Diffraction File 80-965 [21], $a = 3.5925$, $c = 5.1837$), and (101), (200), (105), and (211)—reflections broadening at $2\theta = 25.3$, 48.1, 54.0, and 55.1° for TiO_2 (Powder Diffraction File 84-1286 [21], $a = 3.7822$, $c = 9.5023$). The average values of $[(B^2 - \beta^2)^{0.5}\cos(2\theta/2)]$ for corresponding reflections noted above were used for domain size (h) calculations. The contents of ZrO_2 tetragonal and TiO_2 anatase crystalline phases in Ti(Zr)O_2/SBA-15 composites (C_{XRD}, wt%) were determined based on the summarized integral intensities of all the reflections noted above (I) and wide reflection centered at $2\theta = 23°$ that corresponded to SBA-15 silica (I_0). It was calculated as $C_{XRD} = 100/[(I_0/I) * k + 1]$ where k is the calibration coefficient (1.454 for TiO_2 anatase and 1.735 for tetragonal ZrO_2). Its values were derived from XRD patterns recorded for a series of mechanical mixtures including 5–100 wt% crystalline TiO_2 or crystalline ZrO_2 and SBA-15. The XRD data for (h) and (C_{XRD}) calculations were treated by the Phillips PW187 APO software. The percentage crystallinity of ZrO_2(TiO_2) phases was calculated as $(C_{XRD}/C_{EDS}) * 100$, where C_{EDS} is the concentration of ZrO_2(TiO_2) (wt%) derived from elemental analysis.

HRTEM micrographs were obtained on a JEOL FasTEM-2010 electron microscope operated at 200 kV and equipped with an analytical EDS system for composition analysis. An electron spot probe with a size of ∼ 15–25 nm was used for the determination of the element contents in the material particles by EDS. Phase-contrast HRTEM images from the thinnest areas of the sample were obtained with a removed objective aperture at underfocus conditions close to the Scherzer defocus in order to provide optimum contrast and best resolution. The average size of Pt particles (L) was calculated according to the first moment of distribution $L = \sum n_i * l_i / \sum n_i$, where l is the size of Pt particle determined directly from HRTEM micrograph, and n is the number of particles measured in a specific size. The dispersion of platinum was estimated from the average size of Pt particles according to $D = 6 * (v_m/a_m)/L$, where v_m is the volume occupied by an atom in bulk metal and a_m is the area occupied by a surface atom [24].

Hydrogen thermodesorption spectra (30 cm^3/min Ar, AMI-100, Zeton-Altamira) were recorded in the temperature range 298–673 K after H_2 reduction at 573 K (30 cm^3/min 10 vol%H_2–Ar) and cooling to room temperature in this hydrogen-containing flow.

2.3. Catalysts testing

Oxidation of EA (Aldrich) was studied at atmospheric pressure, 473–623 K, concentration of EA in air 0.5 vol%, and EA $WHSV_{EA} = 2.5$–5 h^{-1}. The experiments were carried out in a stainless-steel 20-mm-i.d. and 30-cm-long tubular reactor. The amount of 0.3 g of catalyst pellets, 0.1–0.2 mm, was diluted with quartz particles of the same size at a 1:5 vol ratio. The concentrations of EA and CO_2 in effluent gas were analyzed on the Varian 3300 GC equipped with a TCD detector and Poropack Q packed column (6 ft, 1/8 in, i.d. 3 mm). At low EA conversions (< 50%) the main products besides CO_2 and water were acetone, acetaldehyde, and acetic acid. The EA conversion (X, %) and CO_2 selectivity (S_{CO_2}, %) were calculated as $X = (1 - C_{EA}/C_{EA_0}) * 100$; $S_{CO_2} = C_{CO_2}/(\varepsilon_{EA} * (C_{EA_0} - C_{EA}) * 100$, where C_{EA} is the concentration of EA in effluent air, C_{EA_0} is the concentration of EA at the reactor inlet, C_{CO_2} is CO_2 concentration at the reactor outlet, and ε_{EA} is the number of carbon atoms in EA molecules. The reaction rate constants of CO_2 formation in oxidation of EA (k_{CO_2}, g g_{cat}^{-1} h^{-1}, g-mass of EA) were calculated based on the first-order kinetics with respect to EA: $-\ln(1 - X/100) = k/WHSV_{EA}$; $k_{CO_2} = S_{CO_2} \cdot k/100$. Turnover frequency (TOF, h^{-1}) was calculated as the amount in moles of EA that was converted to CO_2 per hour divided by the number of moles of exposed Pt surface atoms.

3. Results and discussion

3.1. Characteristics of catalyst samples

Several samples of TiO_2/SBA-15 catalysts with TiO_2 loadings of 44.8–64.1 wt% and ZrO_2/SBA-15 catalysts with ZrO_2 loadings of 48.1–62.1 wt% were prepared by IH and CSD methods. Their characteristics and those of SBA-15 and bulk Ti(Zr)O_2 oxide reference samples after deposition of 0.3 wt% platinum are listed in Table 1. The samples were denoted by their preparation method (CSD, IH, and H) and metal oxide loading in OMS-supported samples. The SAXS patterns of parent SBA-15 displayed three well-defined peaks (100), (110), and (200) of d spacings characteristic of a hexagonal arrangement of cylindrical pores with a distance of 11.9 nm between their axes. The narrow pore-size distribution, derived from N_2-desorption isotherms, was centered at 6.5 nm (5–9 nm range) corresponding to ∼ 5-nm thickness of pore walls. This was also confirmed by the side views of SBA crystals on HRTEM micrographs. According to SEM micrographs the SBA-15 crystals consisted of packages of cylindrical fibers 3–5 μm in diameter. The diameter of one fiber was ∼ 450 nm, length 1–50 μm with ∼ 1500 nanotubes hexagonally packed in every fiber.

Bulk TiO_2 and ZrO_2 reference samples showed TiO_2 anatase or tetragonal ZrO_2 phases (XRD), independent of their preparation method, with crystal sizes of 12–14 nm and surface areas in the range of 50–110 m^2/g (Table 1). Insertion of TiO_2 and ZrO_2 CP into SBA-15 mesopores did not change the peak positions in SAXS patterns but their intensities became strongly reduced. According to Sauer et al. this does not reflect degradation of the SBA-15 structure but is a result of X-ray scattering on inserted CP nanocrystals and reduced SBA-15 concentration in the composites [19]. SEM micrographs also did not indicate any change in the shape of silica fibers forming the SBA-15 crystals after CP inser-

Table 1
Characteristics of catalytic materials after deposition of 0.3 wt% Pt

Sample	TiO_2 or ZrO_2 content (wt%)		SA (m^2/g)		PV	PD	NSA	TiO_2 or ZrO_2		Pt dispersion	TOF
	Total	Anatase or	Total	TiO_2	(cm^3/g)	(average,		(crystal size, nm)		(%)	(h^{-1})
	(C_{XRD})	tetragonal (C_{EDS})		or ZrO_2		nm)		TEM	XRD		
SBA-15	–	–	798	–	1.2	6.0	–	–	–	100	1.4
TiO_2-CSD	100	100	110	110	0.34	12.3	–	–	12	–	–
TiO_2-H	100	100	63	63	0.28	17.7	–	–	12.5	–	–
TiO_2/SBA-CSD40	40	36	445	65[a]	0.45	4.0	0.93	5–10	8.5	83	118
TiO_2/SBA-IH45	45	38	505	117[a]	0.54	5.3	1.14	3–6	5.0	83	222
TiO_2/SBA-IH52	52	46	466	142[a]	0.48	4.1	1.21	3–6	5.0	82	276
TiO_2/SBA-IH64	64	60	391	168[a]	0.39	3.9	1.36	3–6	5.5	81	342
ZrO_2-CSD	100	100	91	91	–	–	–	–	12	–	–
ZrO_2-commercial	100	100	50	50	0.30	24.0	–	–	14	–	–
ZrO_2/SBA-CSD48	48	47	465	108[a]	0.50	4.3	1.12	3–5	4.5	95	74
ZrO_2/SBA-CSD62	62	59	380	136[a]	0.34	3.6	1.22	3–5	4.5	93	119

[a] $SA = 6000 * X/(\rho * d)$, where ρ = theoretical density, d = particle diameter, X = loading.

tion. Well-defined parallel nanotubular channels detected by HRTEM in properly oriented silica fibers of $Ti(Zr)O_2$/SBA-15 confirmed the integrity of SBA-15 structure in CP/SBA-15 composites.

The wide-angle XRD patterns of TiO_2/SBA-15 and ZrO_2/SBA/15 composites contained full sets of peaks corresponding to pure anatase (TiO_2) or tetragonal ZrO_2 phases besides a wide line of amorphous silica centered at $2\theta = 23°$. In the case of ZrO_2 the percentage crystallinity was $> 95\%$ while for TiO_2 it was 85–94% due to strong interactions with SBA-15. The residual part of TiO_2 that could not be detected by XRD probably penetrated into silica pore walls by isomorphous substitution or formed assemblies of TiO_6 tetrahedra grafted at the pore walls as previously shown in [20]. The CP anatase or tetragonal zirconia structure of nanocrystals inside the SBA-15 host was also confirmed by HRTEM. The parallel fringes across the nanocrystals images had a periodicity of 3.55 Å (TiO_2, Fig. 1) or 3.00 Å (ZrO_2) which corresponds to planes with d-spacings $d_{101} = 3.514$ Å or $d_{101} = 2.952$ Å in anatase or tetragonal zirconia structures, respectively [21]. After conversion by Fourier transform into electron diffraction patterns they exhibited sets of diffraction spots that could be indexed on the basis of TiO_2 anatase or tetragonal zirconia unit cell parameters.

No particles with a shape different from that of the packed parallel fibers were detected in $Ti(Zr)O_2$/SBA-15 composites by SEM. Si and Ti or Zr mapping of SEM micrographs showed homogeneous Ti(Zr) distribution in SBA-15 crystals. HRTEM-EDS analysis with an electronic spot 25 nm from different points of the $TiO_2(ZrO_2)$/SBA-15 composites particles gave Ti(Zr) contents similar to those obtained by SEM-EDS. No particles of pure TiO_2 or ZrO_2 were detected outside SBA-15 crystals in composite materials by HRTEM in the micrographs taken from 10 different areas (85×85 μm^2) of the samples. Calcination in air of TiO_2/SBA-15 and ZrO_2/SBA-15 composites up to 1073 K for 2 h did not change the nanocrystals structure and slightly increased the domain size derived from XRD data from 5.0–8.5 to 8–10 for TiO_2 and from 4.5 to 6.5 for ZrO_2. After the same treatment the crystal domain size of bulk reference TiO_2 increased to > 100 nm with full conversion to rutile polymorphs and that of reference bulk ZrO_2 crystals increased to 20–25 nm with partial conversion to monoclinic modification. These SEM, HRTEM, and XRD data together with a substantial shift of the pore diameter to lower values after insertion of $Ti(Zr)O_2$ phases (Table 1) are evidence for location of CP nanocrystals exclusively inside the nanotubes of the SBA-15 host. Moreover, calculation of the normalized surface area of all the composite samples, where $NSA = SA_{composite}/SA_{pure\ SBA\text{-}15}(1 - X)$ and X is $Ti(Zr)O_2$ loading [5], yielded figures which are close or higher than unity (Table 1). It means that the contribution of SBA-15 to the surface area of the $Ti(Zr)O_2$ composite materials pre-

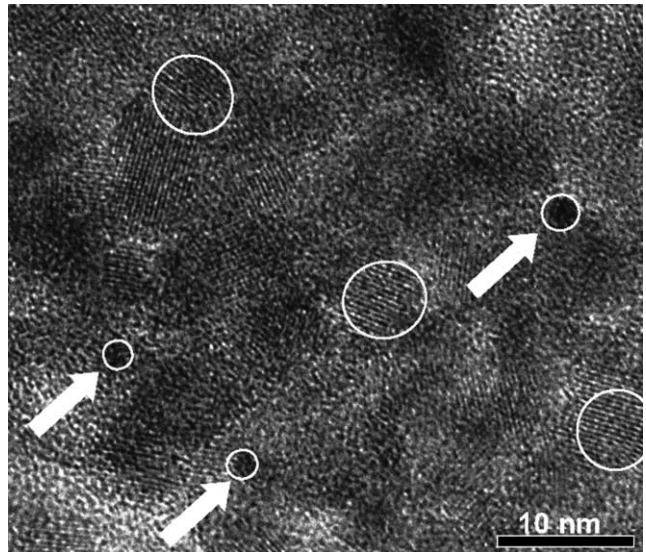

Fig. 1. HRTEM micrograph of Pt/TiO_2/SBA-IH52 sample. TiO_2 particles are marked by white circles while Pt particles are marked by circles with arrows.

pared in the present study corresponds to the original SBA-15 and hence the blocking of the pores is negligible.

Two different types of nanocrystal ensembles were detected inside the silica nanotubes in this study: (I) an ensemble of nanocrystals 4.5–5 nm in size (TiO_2/SBA-15-IH and ZrO_2/SBA-15-CSD), substantially lower than silica nanotubes diameter, and (II) single nanocrystals 8.5 nm size, comparable to the diameter of silica nanotubes (TiO_2/SBA-15-CSD). In addition to the distinction in nanocrystals size (HRTEM, XRD, Table 1) the difference in nanocrystal ensemble types became visualized by figures of the normalized surface area. It was close to unity for type II and higher than unity for type I (Table 1). This reflects the substantial contribution of small nanocrystal ensembles to the total surface area of type I composites, while high values of normalized surface areas are evident for minimal blocking of SBA-15 pores by embedded nanocrystals leaving the surface of Ti(Zr)O_2 CP accessible for adsorbing molecules. It is a consequence of the uniform distribution of Ti(Zr)O_2 nanocrystals along the SBA-15 nanotubular pores clearly observed by HRTEM and conditioned by selected CP insertion strategies. These data allow us to assume minimal agglomeration degrees of CP nanocrystals inside the SBA-15 pore system. Based on such assumption the surface areas of crystalline TiO_2 and ZrO_2 phases were calculated as $SA = 6000 \cdot X/(\rho \cdot d)$, where X is the weight fraction of Ti(Zr)O_2 in composite detected by XRD, ρ is the theoretical density of corresponding crystals (3.9 g/cm^3 for TiO_2 and 5.8 g/cm^3 for ZrO_2), and d is the crystal diameter. The calculated values of metal oxide surface areas in Ti(Zr)O_2/SBA-15 composites are listed in Table 1. Together with reference samples the surface area of corresponding crystalline CP varied for two catalysts sets in range of 63–168 m^2/g for TiO_2 anatase and 50–136 m^2/g for tetragonal ZrO_2.

3.2. Activity and selectivity in EA combustion

All the catalysts listed in Table 1 were tested in EA combustion (Figs. 2 and 3). The light-off curves of EA combustion and CO_2 selectivities measured in a temperature range of 473–633 K for the composite materials displaying the highest surface area of Zr- and Ti-oxide nanocrystals (ZrO_2/SBA-CSD62 and TiO_2/SBA-IH64 with and without Pt, respectively) and for reference Pt/SBA-15 catalyst are shown in Fig. 2. Without platinum both composites displayed low activity and required temperatures > 573 K for visible EA conversion. But even at high temperatures where EA conversions exceed 30% the combustion selectivity to CO_2 was less than 10%, and the main EA conversion route was oxidative degradation forming acetone, acetaldehyde, and acetic acid. The TiO_2/SBA-15 composite showed higher activity in EA degradation compared with its Zr-analogue.

The activity of Pt/SBA-15 catalysts was higher than that of Ti(Zr)/SBA-15 composites with substantially higher combustion selectivity: CO_2 formation became here the main

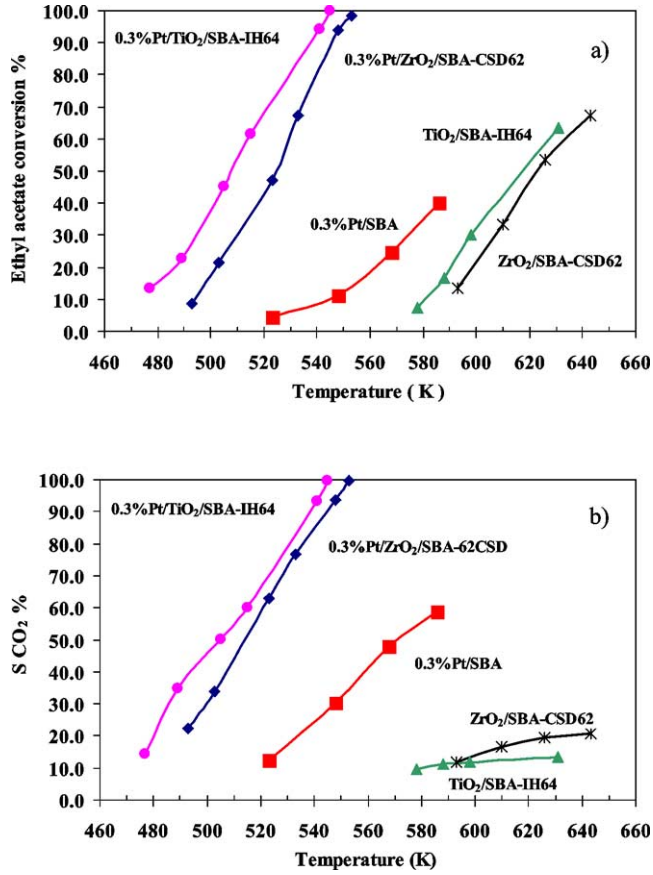

Fig. 2. Light-off curves (a) and CO_2 selectivity (b) of ethyl acetate conversion as a function of temperature measured with Pt/SBA-15, Pt/Ti(Zr)O_2/SBA-15, and Ti(Zr)O_2/SBA-15 at WHSV = 3.3 h^{-1}.

route of EA transformation at conversions > 30%. Addition of platinum to both Ti(Zr)O_2/SBA-15 materials strongly increased the activity and selectivity patterns beyond the level of Pt/SBA-15 catalyst. It shifted the temperature required for > 90% EA conversion to less than 553 K at > 90% combustion selectivity. This strong synergistic effect is attributed to the complementary bifunctional steps of EA transformation occurring on sites of metallic platinum and metal oxide support as was proven before [16,22]. According to [16,22] the EA is cracked on TiO_2 (or ZrO_2) sites into smaller organic molecules which are subsequently oxidized to CO_2 at the Pt surface with much higher rate than noncracked EA. However, our data (Fig. 2) showed that in the absence of platinum not only EA combustion is very poor but also its fragmentation does not occur on Ti(Zr)O_2/SBA-15 catalysts and require much higher temperatures than in the presence of Pt/Ti(Zr)O_2/SBA-15. It means that the nature of the bifunctional effect is more complicated than simple stage separation between Pt and Ti(Zr)O_2 sites. Coexistence of these sites in close vicinity could create the reactive intermediates with high mobility accelerating the EA combustion.

According to the above-noted bifunctional oxidation mechanism, the enhanced activity and selectivity of Pt/Ti(Zr)O_2/SBA-15 catalysts when compared with reference

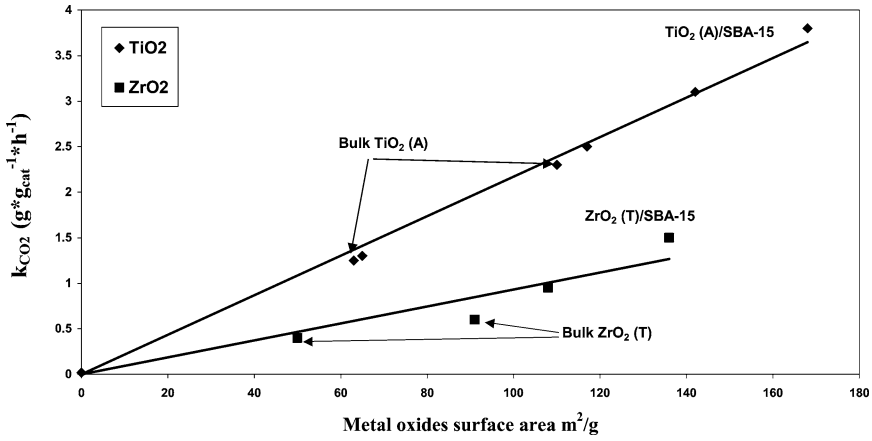

Fig. 3. Effect of surface area of bulk and SBA-15-embedded crystalline Ti(Zr)O_2 phases on supported Pt catalyst activity in ethyl acetate combustion at 523 K.

Pt/SBA-15 (Fig. 2) can be attributed to the addition of oxide which accelerated EA fragmentation or to different dispersions of platinum on the surface which lead to higher combustion activity. Therefore the dispersion of Pt on Pt/Ti(Zr)O_2/SBA-15 and Pt/SBA-15 catalysts was measured as listed in Table 1. Metallic Pt could not be detected in all reduced samples by XRD due to its low content, and high dispersion. Pt dispersion calculated from HRTEM measurements was found to be higher than 80% (corresponding to average Pt particle size in range of 1.2–1.4 nm) in all the samples. H_2-TPD measurements that showed comparable amounts of desorbed hydrogen for both Pt/SBA-15 and Pt/Ti(Zr)O_2/SBA-15 catalysts are also evident for similar Pt dispersion. Previous studies reported that at such high dispersion level the Pt particle-size variation has a negligible effect on VOC combustion rate [25,26]. Therefore, we can conclude that the increase in catalytic performance is due to the contribution of Ti(Zr)-oxides to the catalytic cycle of EA combustion in agreement with the functional mechanism discussed above. This was also confirmed by the increase of turnover frequencies of CO_2 formation on supported Pt in a range of more than two orders of magnitude after insertion of ZrO_2 or TiO_2 into SBA-15 (Table 1). The bifunctional oxidation mechanism with EA fragmentation at the surface of Ti(Zr)O_2 as a limiting step followed by fast combustion of light hydrocarbons on Pt is consistent also with observed correlation between the EA fragmentation activity of Ti(Zr)O_2/SBA-15 and EA combustion efficiency of their platinized analogs (Fig. 2).

Plotting the rate constants of CO_2 formation (complete EA oxidation) calculated for the two sets of Ti and Zr catalysts at 523 K versus the specific surface area of crystalline anatase or tetragonal zirconia phases in supported Pt catalysts yielded linear trends (Fig. 3). The zero point of these plots was fixed at $k_{CO_2} = 0.019\ \mathrm{g\,g_{cat}^{-1}\,h^{-1}}$ measured with the reference catalyst 0.3%Pt/SBA-15 in the absence of transition metal oxides. Growing the surface area of Ti- or Zr-oxide proportionally increased the rate of EA combustion ($k_{CO_2} = \alpha \cdot \mathrm{SA}_{\mathrm{TiO_2(ZrO_2)}}$) with a proportionality factor of $\alpha = 2.2 \times 10^{-2}\ \mathrm{g\,h^{-1}\,m^{-2}}$ for TiO_2 and $\alpha = 0.9 \times 10^{-2}\ \mathrm{g\,h^{-1}\,m^{-2}}$ for ZrO_2 (Fig. 3). The linear trends presented in Fig. 3 clearly demonstrate that the EA combustion rate with platinized Ti(Zr)O_2-based catalysts is determined by the surface area of crystalline Ti(Zr)O_2 phases. The lower efficiency of ZrO_2-based support could be attributed to its lower activity in EA degradation (Fig. 2). The linear trends shown in Fig. 3 included bulk TiO_2 and ZrO_2 samples tested in the form of pellets 0.1–0.2 mm that excluded the diffusion limitations of reaction rate. The fact that k_{CO_2} values measured with Pt/Ti(Zr)O_2/SBA-15 catalysts fall on the same lines with bulk samples is evidence of the absence of diffusion limitations also with embedded CP and their full accessibility for reacting molecules. The lack of pore blocking was previously confirmed by N_2-adsorption data.

Insertion inside the SBA-15 host allowed stabilizing the small nanocrystals of active TiO_2 or ZrO_2 polymorphs at high temperatures needed for their formation. It yielded active crystalline metal oxide CP with surface areas of 308 (TiO_2) or 228 (ZrO_2) $\mathrm{m^2/g_{Ti(Zr)O_2}}$ calculated based on the phase densities and crystal size. Even after dilution with SBA-15 silica the surface area of accessible CP and the activity of Pt catalysts in EA combustion are 1.7–3 times higher than those measured with bulk transition metal oxides. This demonstrates the advantage of CP/OMS composites as catalytic materials for VOC combustion. The value of k_{CO_2} measured at 523 K with a Pt catalysts deposited on commercial alumina support (0.3%Pt/γ-Al_2O_3) widely used for VOC combustion was $0.040\ \mathrm{g\,g_{cat}^{-1}\,h^{-1}}$. This is two orders of magnitude less compared with the most active Pt/TiO_2/SBA-15 catalyst tested in the present study.

4. Conclusions

Chemical solution decomposition and hydrolysis of Ti- and Zr-alcoxides inside the nanotubular pores of mesostructured SBA-15 silica allow insertion of up to 65 wt% transition metal oxide as 4.5–8.5 nm nanocrystals located exclusively inside the mesopores. The Ti(Zr)O_2 nanocrystals

are uniformly distributed along nanotubes of mesostructured silica hosts and does not block them. The embedded $Ti(Zr)O_2$ nanocrystals demonstrate high thermal stability and at $\sim$60 wt% loadings displayed surface areas of 308 (TiO_2) or 228 (ZrO_2) $m^2/g_{Ti(Zr)O_2}$—1.7–3 times higher than bulk oxides prepared under the same conditions. After Pt deposition the activity of $Ti(Zr)O_2$/SBA-15 materials in ethylacetate combustion was proportional to the surface area of corresponding transition metal oxides, being a function of their loading and crystal size.

Acknowledgments

This study was supported by the Israel Science Foundation, Center of Excellence (Grant No 8003). The authors gratefully acknowledge Mr. V. Ezersky for conducting the HRTEM experiments.

References

[1] U. Ciesla, F. Schüth, Micropor. Mesopor. Mater. 27 (1999) 131.
[2] G.J. de Soler-Illia, C. Sanchez, B. Lebeau, J. Patarin, Chem. Rev. 102 (2002) 4093.
[3] F. Schüth, W. Schmidt, Adv. Eng. Mater. 4 (5) (2002) 269.
[4] D. Brunel, A.C. Blank, A. Galarnea, F. Fajula, Catal. Today 73 (2002) 139.
[5] L. Vradman, M.V. Landau, M. Herskowitz, V. Ezersky, M. Talianker, S. Nikitenko, Y. Koltypin, A. Gedanken, J. Catal. 213 (2003) 163.
[6] A. Wingen, N. Anastasievič, A. Hollnagel, D. Werner, F. Schüth, J. Catal. 193 (2000) 248.
[7] M.V. Landau, L. Titelman, L. Vradman, P. Wilson, Chem. Commun. (2003) 594.
[8] Hai-Ou-Zhu, Jun Wang, Chong-Yu Zeng, Dong-Yuan Zhao, Stud. Surf. Sci. Catal. 146 (2003) 661.
[9] Yu-Hsiang Hsien, Chi-Fu Chang, Yu-Huang Chen, Soofin Cheng, Appl. Catal. B 31 (2001) 241.
[10] A.A. Belhekar, S.V. Awate, R. Anand, Catal. Commun. 3 (2002) 453.
[11] R. van Grieken, J. Aguado, M.J. Lopez-Muñoz, J. Marugan, J. Photochem. Photobiol. A 148 (2002) 315.
[12] Z. Zhang, C.C. Wang, R. Zakaria, J.Y. Ying, J. Phys. Chem. B 102 (1998) 10871.
[13] C.B. Almquist, P. Biswas, J. Catal. 212 (2) (2002) 145.
[14] B.K. Hodnett, in: Heterogeneous Catalytic Oxidation, Fundamentals and Technological Aspects of the Selective and Total Oxidation of Organic Compounds, Willey, Chichester, 2000, pp. 191–199.
[15] H. Rotter, M.V. Landau, M. Carrera, D. Goldfarb, M. Herskowitz, Appl. Catal. B 47 (2004) 111.
[16] P. Papaefthimiou, T. Ioannides, X.E. Verykios, Appl. Catal. B 15 (1998) 75.
[17] K. Okumura, T. Kobayashi, H. Tanaka, M. Niwa, Appl. Catal. B 44 (2003) 325.
[18] D. Zhao, J. Sun, Q. Li, G.D. Stucky, Chem. Mater. 12 (2000) 275.
[19] J. Sauer, F. Marlow, F. Schüth, Phys. Chem. Chem. Phys. 3 (2001) 3679.
[20] A. Tuel, L.G. Hubert-Pfalzgraf, J. Catal. 217 (2003) 343.
[21] Powder Diffraction Files, JCPDS, International Center for Diffraction Data, 1984.
[22] J.E. Sawyer, M.A. Abraham, Ind. Eng. Chem. Res. 33 (1994) 2084.
[23] N.S. Resende, J.G. Eon, M. Schmal, J. Catal. 183 (1999) 6.
[24] G. Bergeret, P. Gallezot, in: G. Ertl, H. Knozinger, J. Weitkamp (Eds.), Handbook of Heterogeneous Catalysis, Willey, Weinheim, 1997, p. 439.
[25] Y.F. Yu Yao, Ind. Eng. Chem. Product Res. Dev. 19 (1980) 293.
[26] A. O'Malley, B.K. Hodnett, in: Proceedings of 4th World Congress on Oxidation Catalysis, Berlin/Potsdam (September 2001), Dechema, 2001, p. 1275.